Available online at www.sciencedirect.com
ScienceDirect
Ocean Modelling 20 (2008) 183–206
Ocean Modelling
www.elsevier.com/locate/ocemod

Very large eddy simulation of the Red Sea overflow

Mehmet Ilıcak [a,*], Tamay M. Özgökmen [a], Hartmut Peters [a], Helmut Z. Baumert [b], Mohamed Iskandarani [a]

[a] 4600 Rickenbacker Causeway, MPO/RSMAS, 33149 Miami, FL, USA
[b] Institute for Applied Marine and Limnic Studies, Hamburg, Germany

Received 5 June 2007; received in revised form 29 August 2007; accepted 30 August 2007
Available online 25 September 2007

Abstract

Mixing between overflows and ambient water masses is a critical problem of deep-water mass formation in the downwelling branch of the meridional overturning circulation of the ocean. Modeling approaches that have been tested so far rely either on algebraic parameterizations in hydrostatic ocean circulation models, or on large eddy simulations that resolve most of the mixing using nonhydrostatic models.

In this study, we examine the performance of a set of turbulence closures, that have not been tested in comparison to observational data for overflows before. We employ the so-called very large eddy simulation (VLES) technique, which allows the use of k–ε models in nonhydrostatic models. This is done by applying a dynamic spatial filtering to the k–ε equations. To our knowledge, this is the first time that the VLES approach is adopted for an ocean modeling problem.

The performance of k–ε and VLES models are evaluated by conducting numerical simulations of the Red Sea overflow and comparing them to observations from the Red Sea Outflow Experiment (REDSOX). The computations are constrained to one of the main channels transporting the overflow, which is narrow enough to permit the use of a two-dimensional (and nonhydrostatic) model. A large set of experiments are conducted using different closure models, Reynolds numbers and spatial resolutions.

It is found that, when no turbulence closure is used, the basic structure of the overflow, consisting of a well-mixed bottom layer (BL) and entraining interfacial layer (IL), cannot be reproduced. The k–ε model leads to unrealistic thicknesses for both BL and IL, while VLES results in the most realistic reproduction of the REDSOX observations.

Keywords: Very large eddy simulation; Red Sea overflow; k–ε turbulence model; Entrainment

1. Introduction

The understanding of the meridional overturning circulation (MOC) is important in order to quantify the role of the ocean in climate dynamics, and overflows associated with high-latitude and marginal seas play a major role in the downwelling branch of this circulation. The strength of the MOC is thought to be sensitive

* Corresponding author.
E-mail address: milicak@rsmas.miami.edu (M. Ilıcak).

1463-5003/$ - see front matter © 2007 Elsevier Ltd. All rights reserved.
doi:10.1016/j.ocemod.2007.08.002

to deep-water formation taking place mainly in polar seas by cooling (e.g., Dickson et al., 1990) and in marginal seas by evaporation (e.g., the Mediterranean Sea; Baringer and Price, 1997 and the Red Sea; Bower et al., 2005). The overflows form one of the bottle necks in the MOC because the modification of the properties of the *source* waters, bottom water in marginal or polar 4s, to the *product* waters, the waters released into the general circulation (Price and Baringer, 1994). The modification happens over much smaller spatial and temporal scales than those associated with the MOC. In the downwelling branch of the MOC, most of the deep and intermediate water masses in the ocean can be traced to a few major overflows (Warren, 1981), those from the Mediterranean Sea, the Denmark Strait, the Faroe Bank Channel, the Red Sea and the Antarctic Slope. These major overflows have been studied via observational programs (Baringer and Price, 1997; Girton et al., 2001; Peters et al., 2005b, 2004). One of the primary findings that is common in all these observational programs performed in the major overflows is that small-scale mixing and ambient stratification determine the product water properties.

Small-scale mixing is thought to arise on the one hand due to shear instabilities taking place between rapidly propagating (typically $\sim 1\ \mathrm{m\,s^{-1}}$) bottom gravity currents and the ambient fluid, and on the other hand due to the action of various forms of non-linear internal waves (mainly their breaking). The separation of scales between those of overflow mixing and the MOC is such that not all scales of motion can be numerically integrated simultaneously due to computational expense. This becomes particularly challenging as the domain size gets larger, for instance in global models used in climate studies (Griffies et al., 2000). As such, parameterizations of overflow processes need to be developed, and it seems critical to represent as realistically as possible the net effect of small-scale mixing in these parameterizations.

There are different approaches to develop parameterizations of overflow mixing. The *first* is to systematically perform laboratory experiments of bottom gravity currents (e.g. Ellison and Turner, 1959; Hallworth et al., 1996; Baines, 2001; Cenedese et al., 2004; Baines, 2005). Their main advantage is that large ensembles of experiments can be conducted with known parameters. The disadvantages include the fact that the effective Reynolds number is orders of magnitude smaller and the topographic slopes are typically much larger than those in the ocean (or simply that oceanic overflows cannot be fit in a tank of a few meters size), and that it is not trivial to measure all prognostic flow variables (in particular the velocity distribution) at high resolutions. Laboratory experiments are useful in understanding many of the key features of bottom gravity currents (Simpson, 1987), as well as for developing parameterizations of mixing in early models of overflows (Killworth, 1977).

The *second* approach to develop parameterizations of overflow mixing is using high resolution numerical models, and this became possible by the improvement of computer power. By recognizing that the resolution of stratified overturning eddies (such as Kelvin–Helmholtz rollers) would be critical step in representing the overflow mixing, a number of studies with numerical models integrating Boussinesq equations (or so-called nonhydrostatic models) have been conducted. Idealized bottom gravity currents are simulated in 2D and 3D settings over smooth topography (Özgökmen and Chassignet, 2002; Özgökmen et al., 2004b), over complex topography (Özgökmen et al., 2004a) and in the presence of ambient stratification (Özgökmen et al., 2006). These studies belong to the category of large eddy simulation (LES), in which the energy containing flow structures are resolved in time and space, and the effect of smaller eddies on the resolved fields is represented by sub-grid scale (SGS) models. The underlying assumption of LES is that large eddies carry most of the Reynolds stress and are specific to the type of turbulent flows, and thus must be resolved. On the other hand, small-scale eddies contribute much less to Reynolds stress and have a more universal role, and thus can be parametrized.

When compared to direct numerical simulation (DNS), in which all scales of motion are resolved and closure assumptions are not needed, LES employs simple SGS closure models and offers significant computational gains (or larger domain size). While most of the SGS model development has been traditionally focused on homogeneous fluids (Sagaut, 2005), it was shown recently that simple forms work reasonably well in stratified flows, provided that the largest overturning (Ozmidov) scale is resolved (Özgökmen et al., 2007).

In contrast to LES, the parameterization of sub-grid scale mixing is much more crucial in ocean general circulation models (OGCMs). This is because OGCMs employ the hydrostatic approximation with coarse mesh sizes. As such, vertical overturning eddies (thus mixing) due to shear instabilities, such as Kelvin–Helmholtz vortices, are not captured. Thus, OGCMs must rely entirely on the accuracy of vertical (or diapycnal) parameterizations to capture overflow mixing.

These parameterizations can be broadly classified into *diagnostic* and *prognostic*. In diagnostic models, vertical viscosity and diffusivity are expressed as algebraic functions of the hydro-thermodynamic mean fields (e.g. Large et al., 1994; Large and Gent, 1999; Hallberg, 2000; Chang et al., 2005, 2006). Mixing models of this type are computationally inexpensive. The prognostic models are essentially based on one or more differential equations. The majority of today's closure models rests on the Reynolds decomposition of the state variables into mean and fluctuating (or turbulent) components and averaging of the Navier–Stokes equations (RANS). The eddy viscosity and diffusivity are expressed as a function of two turbulent prognostic fields, such as the turbulent kinetic energy k and a turbulent length scale l, or dissipation rate ε, or frequency ω.

There has been a steady improvement in turbulent closure models used in oceanographic applications (Rodi, 1980; Mellor and Yamada, 1982; Baumert and Radach, 1992; Kantha and Clayson, 1994; Burchard and Baumert, 1995; Canuto et al., 2001; Baumert and Peters, 2004; Umlauf and Burchard, 2005; Peters et al., 2005a; Baumert et al., 2005). The so-called Mellor–Yamada model (Mellor and Yamada, 1982) has been used in overflow studies by Jungclaus and Mellor (2000), Ezer and Mellor (2004), Ezer (2005) and Ezer (2005) compared results from a 2.5 km resolution hydrostatic model using Mellor–Yamada turbulence closure to those from a 0.5 km resolution nonhydrostatic model for an idealized overflow problem. They found that results from nonyhdrostatic and hydrostatic models are similar and they concluded that given enough resolution hydrostatic models with two-equation turbulence closures can simulate the sub-grid scale mixing quite well. A hydrostatic model with Mellor–Yamada turbulence closure is also compared with the observational data. Specifically, Ezer (2006) simulated an idealized Faroe Bank Channel overflow using a high resolution hydrostatic model, and compared with the field observations of Mauritzen et al. (2005) and Geyer et al. (2006).

A challenge is posed by the steady increase in the computational power:

> How can the physical insight and progress attained by decades-long developments in turbulence closures be incorporated in an LES model, which is already partially resolving the flow turbulence?

This is the main motivation behind so-called Very Large Eddy Simulation (VLES), which can be considered as a combination of LES and RANS. In VLES, only the very large turbulent structures are resolved and the remaining turbulence is parameterized. Since a wider range of scales is modeled in VLES than in LES, the SGS models need to be more comprehensive, and thus turbulence closures developed in the context of RANS provide an attractive solution. The main concepts behind LES, RANS and VLES are summarized in Fig. 1. The VLES approach has been used by Magagnato and Gabi (2002) and Ruprecht et al. (2003) for engineering applications and shown to provide better results than RANS models. This is because the mean flow is either independent of time or slowly varying in RANS, and conventional turbulence models using RANS are insufficient for unsteady flows when the turbulent time scale has the same order of buoyancy time scale (i.e. $T \sim N^{-1}$). VLES is designed to capture and model the turbulence in transient flows.

Based on the above review, a number of questions can be posed:

- Are SGS models really needed in nonhydrostatic simulations of overflows?
- How well would the RANS models work in overflow simulations?
- What is the value of VLES in reproducing overflow mixing?
- How do the performance of RANS and VLES change and differ as a function of model spatial resolution?

The main objective of this study is to address these questions. To this end, numerical simulations are carried out using both RANS and VLES approaches with a nonhydrostatic model. In order to assess the importance of the turbulence closure terms, the model is integrated without closures as well, corresponding to so-called under-resolved DNS. The accuracy of the results is evaluated using hydrographic data collected in the Red Sea Outflow Experiment (REDSOX, Peters and Johns, 2005; Peters and Johns, 2006; Bower et al., 2005). To our knowledge, this is the first time that the performance of prognostic turbulence closure models for overflow mixing has been carefully evaluated using observational data, and also the first time that VLES approach is adapted for an oceanographic flow simulation.

This paper is organized as follows: The REDSOX observational program is briefly discussed in Section 2. The numerical model and turbulence closures are introduced in Section 3. The setup of the numerical

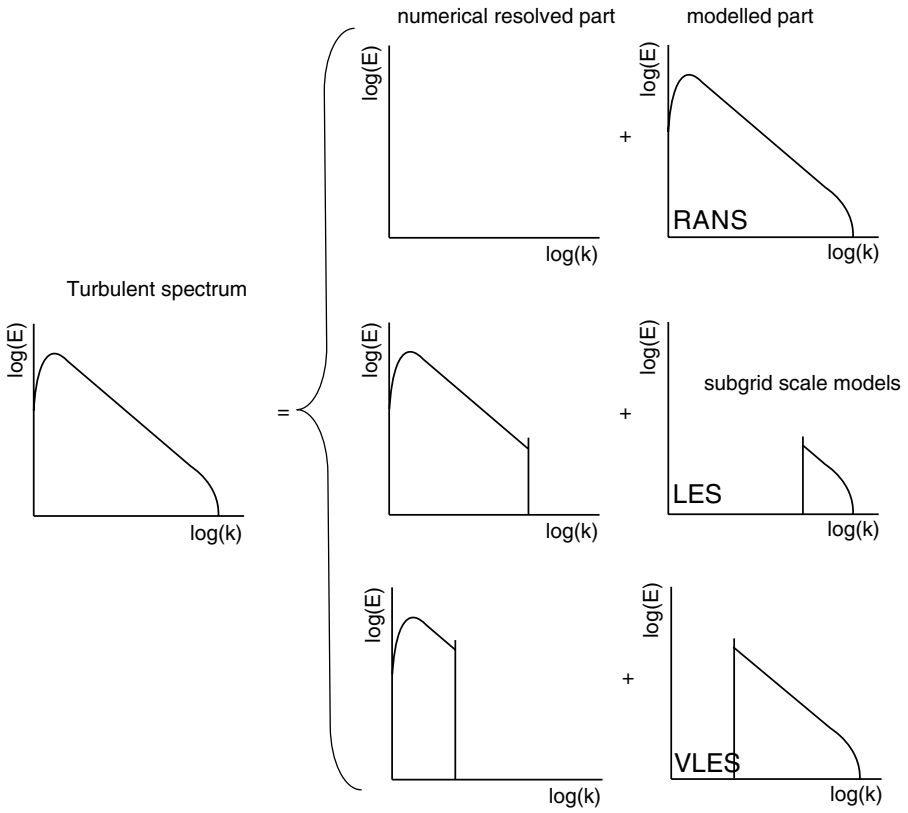

Fig. 1. Schematic description of the concepts behind RANS, LES and VLES. The energy containing vertical scale is the Ozmidov scale in a stratified flow, and the smallest dynamical scale is the Kolmogov scale.

experiments and model parameters are outlined in Section 4. The evaluation strategy is described in Section 5. The main results are presented in Section 6. Finally we summarize and conclude in Section 7.

2. Main characteristics of the Red Sea outflow

Here we summarize the relevant findings from the Red Sea Outflow Experiment (REDSOX). The reader is referred to Bower et al. (2002), Peters and Johns (2005), Bower et al. (2005), Peters and Johns (2006), Peters et al. (2005b) and Matt and Johns (2007) for the complete analysis of the observational results. REDSOX was a joint program between Rosenstiel School of Marine and Atmospheric Science and the Woods Hole Oceanographic Institution to understand the structure, dynamics, mixing of the Red Sea overflow. Two cruises were performed in 2001, one in the winter (REDSOX-1) when the outflow is maximum and one in the summer (REDSOX-2) when the outflow is minimum. The pronounced seasonal variability of the outflow from the Red Sea (Murray and Johns, 1997) is a consequence of the monsoon circulation over the northwestern Indian Ocean and adjacent land areas. The MOC may be strongly affected by the major overflows such as the Denmark Strait overflow, Faroe Bank Channel overflow and the Antarctic overflows. Although the volume transport of the Red Sea overflow water is the smallest one compared to these major overflows (around annual mean of just 0.37 Sv from Murray and Johns, 1997), observations taken throughout the Indian Ocean during the World Ocean Circulation Experiment shows that Red Sea overflow water has a distinctive and far reaching signal. The influence of Red Sea overflow water has been measured in the Agulhas Current, and also in the Agulhas retroflection region to the south of South Africa (Beal et al., 2000). Red Sea deep water is formed at the northern edge of the Red Sea (Morcos, 1970; Sofianos and Johns, 2001), and this dense, warm and salty water flows south through the narrow strait of Bab el Mandeb. According to observations, the outflow south

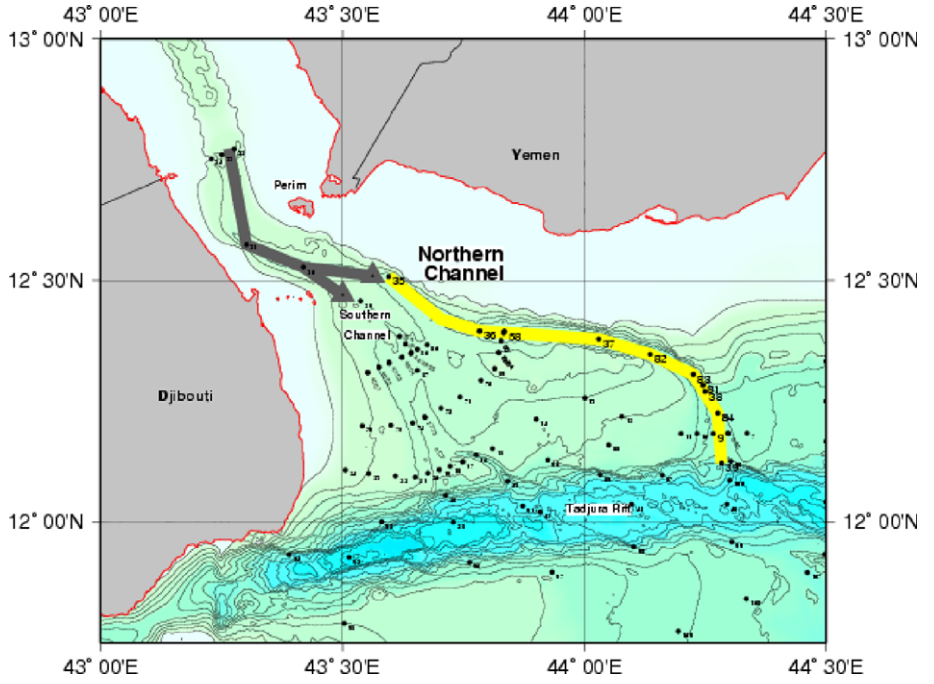

Fig. 2. Northern (highlighted) channel of the Red Sea, and locations of plume survey stations from REDSOX cruises.

of Bab el Mandeb divides into two channels, the typically 5 km wide and 130 km long "northern" channel and the "southern" channel which is wider and shallower than the northern one (Fig. 2).

In the present study, we carry out numerical simulations of the part of the Red Sea overflow confined to the northern channel. This is because the northern channel is narrow and helps reduce the spreading, lateral mixing and instabilities in the overflow. As such, the overflow dynamics are approximated using a 2D model. Furthermore, the northern channel overflow has been more extensively observed, and its key features are better known than those of the southern channel overflow. In particular, Peters et al. (2005b) put forth that the structure of the overflow in both channels consists of two dynamically different components: the bottom layer (BL), and the interfacial layer (IL). The former reaches from the bottom to the point where the velocity is maximum, and the latter is located between the velocity maximum and the ambient fluid. The BL is well mixed and maintains high salinities along the northern channel, while the IL is characterized by strong density gradients and high shear. In particular, the ratio of stratification to shear leads to low Richardson numbers in the IL. Most of the mixing and overturns occur in the IL. As such, it is important to capture the BL and the IL in the numerical simulations in order to achieve a faithful reproduction of the characteristics of the northern channel overflow.

3. The numerical model

3.1. The 2D Reynolds solver

In this study, a 2D Boussinesq (nonhydrostatic) model is used since the northern channel is narrow enough to naturally restrict motions in the lateral direction. Furthermore, the width of the channel is much smaller than the Rossby radius of deformation and the channel length. Thus, the effects of baroclinic instability and rotation on the overflow dynamics are assumed to be small, and neglected. The 2D model is based on vorticity–streamfunction formulation, and the governing equations are nondimensionalized as follows:

$$\psi = U_0 h \psi^*, \quad (x,z) = h(x^*,z^*), \quad \zeta = (U_0/h)\zeta^*,$$
$$S = (\Delta S)S^*, \quad T = (\Delta T)T^*, \quad t = (h/U_0)t^*.$$

Here ψ is the stream function, ζ is the vorticity, h is the thickness of the overflow at the inlet, ΔS and ΔT are the ranges of salinity and temperature in the system obtained from REDSOX data, and U_0 is the characteristic velocity scale of the Red Sea overflow, 1 m s^{-1}. Dimensional mean velocities ($\overline{U}$(m/s) and $\overline{W}$(m/s)) are defined and nondimensionalized as:

$$\overline{U} = -\frac{\partial \psi}{\partial z} = U_0 \overline{U}^* \quad \text{and} \quad \overline{W} = \frac{\partial \psi}{\partial x} = U_0 \overline{W}^*.$$

Asterisks and bars are dropped for simplicity, and the final forms of the streamfunction, vorticity, salinity and temperature equations are (henceforth RAVS will be used for Reynolds Averaged Vorticity Streamfunction equations)

$$\frac{D\zeta}{Dt} = \frac{1}{Fr^2}\left(R_\rho \frac{\partial T}{\partial x} - \frac{\partial S}{\partial x}\right) + \frac{1}{Re}\nabla^2\zeta + \frac{\partial}{\partial x}\left(\frac{1}{Re_t}\frac{\partial \zeta}{\partial x}\right) + \frac{\partial}{\partial z}\left(\frac{1}{Re_t}\frac{\partial \zeta}{\partial z}\right), \tag{1}$$

$$\frac{DT}{Dt} = \frac{1}{RePr}\nabla^2 T + \frac{\partial}{\partial x}\left(\frac{1}{Re_t Pr_t}\frac{\partial T}{\partial x}\right) + \frac{\partial}{\partial z}\left(\frac{1}{Re_t Pr_t}\frac{\partial T}{\partial z}\right), \tag{2}$$

$$\frac{DS}{Dt} = \frac{1}{RePr}\nabla^2 S + \frac{\partial}{\partial x}\left(\frac{1}{Re_t Pr_t}\frac{\partial S}{\partial x}\right) + \frac{\partial}{\partial z}\left(\frac{1}{Re_t Pr_t}\frac{\partial S}{\partial z}\right), \tag{3}$$

$$\nabla^2\psi = \zeta, \tag{4}$$

where $Re = U_0 h/\nu$ is the Reynolds number, the ratio of inertial to viscous forces, and $Fr = U_0/\sqrt{g\beta\Delta S h}$ is the Froude number, the ratio of the inertial to gravitational forces in the flow; $g = 9.81$ m s^{-2} is the gravitational acceleration, $R_\rho \equiv \alpha\Delta T/\beta\Delta S$ is the density ratio, quantifying influence of temperature and salinity on density respectively, where α is the temperature expansion coefficient and β is the salinity contraction coefficient for seawater in the linear equation of state $\rho = \rho_0(1 - \alpha\Delta T + \beta\Delta S)\cdot Pr = \nu/K$ is the molecular Prandtl number, the ratio of (molecular values of) viscosity to diffusivity, ∇^2 is the Laplace operator, and the material derivative of the vorticity equation is

$$\frac{D\Phi}{Dt} = \frac{\partial \Phi}{\partial t} + J(\psi, \Phi).$$

The Jacobian, $J(\psi, \Phi)$,

$$J(a,b) = \frac{\partial a}{\partial x}\frac{\partial b}{\partial z} - \frac{\partial b}{\partial x}\frac{\partial a}{\partial z},$$

is discretized using the Arakawa (1966) scheme to conserve both energy and entrophy. Re_t is the turbulent Reynolds number which is computed from the turbulence closure models, and Pr_t is the turbulent Prandtl number, discussed below. The last two terms on the right hand side of the Eqs. (1)–(3) contain the turbulent fluxes. In the limit of very high Re (typical of oceanic parameter range), the contributions of the second term on the rhs of Eq. (1) and the first terms on the rhs of Eqs. (2) and (3) become much smaller with respect to the turbulent fluxes. Nevertheless, it is important to include these terms for consistency.

A conformal mapping is used to convert complex topography in physical coordinates (x, z) into a rectangular domain in computational coordinates (ξ, η) (Figs. 3 and 4). The ensuing equations are discretized with finite differences. The Poisson Equation (4) is solved using direct a Fast Fourier transform, which is not only a more accurate method than iterative solution techniques, but also faster for a large number of discretization points. The vorticity equation (1) is advanced in time using Adams–Bashforth-3 method. Temperature and

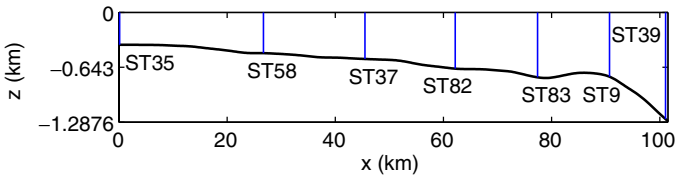

Fig. 3. Model domain size, topography, locations and numbers of the observational stations.

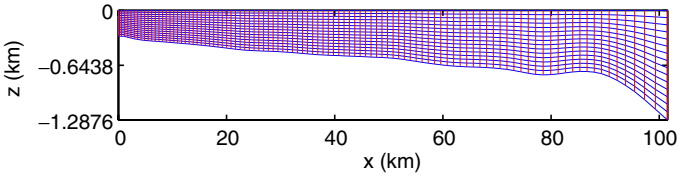

Fig. 4. Sample model domain discretization using 101 × 16 (on average $\Delta x \approx 1000$ m, and $\Delta z \approx 66$ m) points with conformal mapping.

salinity transport equations (2) and (3) rely on Flux Corrected Transport Zalesak method to eliminate Gibbs oscillations (Zalesak, 1978).

3.2. The closures

In this study, two different closure models are applied. The first one is the k–ε model based on Baumert and Peters (2000), Peters et al. (2005a) and Warner et al. (2005). The second is VLES.

3.2.1. The k–ε closure model

Turbulent kinetic energy, k, and its dissipation rate, ε, are nondimensionalized by $k = U_0^2 k^*$, and $\varepsilon = (U_0^3/h)\varepsilon^*$, respectively. The asterisks are omitted for simplicity. The transport equations for nonndimensional turbulent kinetic energy and the dissipation rate are then given by

$$\frac{\mathrm{D}k}{\mathrm{D}t} = P + B - \varepsilon + \frac{1}{Re}\nabla^2 k + \frac{\partial}{\partial x}\left(\frac{1}{Re_t \sigma_k}\frac{\partial k}{\partial x}\right) + \frac{\partial}{\partial z}\left(\frac{1}{Re_t \sigma_k}\frac{\partial k}{\partial z}\right), \tag{5}$$

$$\frac{\mathrm{D}\varepsilon}{\mathrm{D}t} = \frac{\varepsilon}{k}\left[c_{\varepsilon 1}(P + c_{\varepsilon 3}B) - c_{\varepsilon 2}\varepsilon\right] + \frac{\nabla^2 \varepsilon}{Re} + \frac{\partial}{\partial x}\left(\frac{1}{Re_t \sigma_\varepsilon}\frac{\partial \varepsilon}{\partial x}\right) + \frac{\partial}{\partial z}\left(\frac{1}{Re_t \sigma_\varepsilon}\frac{\partial \varepsilon}{\partial z}\right). \tag{6}$$

In the Eqs. (5) and (6), P is the production term due to shear forces, and B is due to buoyancy forces,

$$P = \frac{1}{Re_t}\left[\left(\frac{\partial U}{\partial z} + \frac{\partial W}{\partial x}\right)^2 + 2\left(\frac{\partial U}{\partial x}\right)^2 + 2\left(\frac{\partial W}{\partial z}\right)^2\right], \tag{7}$$

$$B = \frac{1}{Fr^2 Re_t Pr_t}\left(\frac{\partial S}{\partial z} - R_\rho \frac{\partial T}{\partial z}\right). \tag{8}$$

The coefficients used in this k–ε model are listed in Table 1.

The turbulent Reynolds number, Re_t, and turbulent Prandtl number, Pr_t, are defined as

$$Re_t \equiv \left(c_\mu \frac{k^2}{\varepsilon}\right)^{-1}, \tag{9}$$

$$Pr_t \equiv \frac{S_M}{S_H}, \tag{10}$$

where S_H and S_M are the stability functions taken from Kantha and Clayson (1994) and Warner et al. (2005),

Table 1
Coefficients used in k–ε Eqs. (5) and (6)

σ_k	σ_ε	$c_{\varepsilon 1}$	$c_{\varepsilon 2}$	$c_{\varepsilon 3}$	c_μ
1.0	1.3	1.44	1.92	−1.0	0.09

$$S_H = \frac{A_2(1 - 6A_1/B_1)}{1 - 3A_2G_h(6A_1 + B_2(1 - C_3))}, \tag{11}$$

$$S_M = \frac{B_1^{-1/3} + (18A_1A_1 + 9A_1A_2(1 - C_2))S_HG_h}{1 - 9A_1A_2G_h}, \tag{12}$$

$$G_h = \frac{G_{h\_\text{unlimit}} - (G_{h\_\text{unlimit}} - G_{h\_\text{crit}})^2}{G_{h\_\text{unlimit}} + G_{h0} - 2G_{h\_\text{crit}}}, \tag{13}$$

$$G_{h\_\text{unlimit}} = -\frac{N^2L^2}{2k}, \tag{14}$$

where N is the buoyancy frequency, and L is the length scale of the energy containing eddies defined as

$$L = c_1\frac{k^{3/2}}{\varepsilon}, \tag{15}$$

where c_1 may have a wide range, from 0.161 (Baumert and Peters, 2000) to 1 (Buntić et al., 2006). In this study c_1 is taken as 1. Parameters used in stability functions are given in Table 2. Further information about the stability functions (such as plots of S_H, S_M versus G_h, and variation of S_H, S_M with flux Richardson number) can be found in Kantha and Clayson (1994).

3.2.2. VLES closure model

The second turbulence closure model is VLES. In this model, part of the turbulence spectrum can be resolved, and the influence of the unresolved part on the resolved part has to be modeled. In order to distinguish the resolved and the modeled parts, a spatial filtering technique is used (Buntić et al., 2006). In this method a length scale filter, δ, is applied to the standard k–ε closure. This length scale depends on either the computational time step and local velocity or local grid size. For the turbulent kinetic energy, large scales are already resolved and the small scales are filtered and obtained from

$$\hat{k} = \begin{cases} k & \text{if } \delta \geqslant L, \\ (\delta\varepsilon)^{2/3} & \text{if } \delta < L, \end{cases} \tag{16}$$

where the hat symbol, "$\hat{}$", represents spatial filtering and

$$\delta = \alpha \cdot \max\begin{cases} |u| \cdot \Delta t \\ \sqrt{\Delta V} \end{cases}, \tag{17}$$

where $\alpha = 2$ is a model constant, u is the local velocity, Δt is the computational time step, and ΔV is the local volume (i.e. area in 2D). According to Kolmogorov (1942) theory, the dissipation rate is constant for all scales in the whole spectrum, which leads to

$$\varepsilon = \hat{\varepsilon}. \tag{18}$$

The filtered turbulent kinetic energy, $\hat{k}$, and its dissipation rate, $\hat{\varepsilon}$, were resubstituted into the Eqs. (5) and (6), and turbulent Reynolds number computed as

$$Re_t \equiv \left(c_\mu\frac{\hat{k}^2}{\hat{\varepsilon}}\right)^{-1}. \tag{19}$$

The same stability functions are also used in VLES. Thus, the filtering procedure (16) is the only difference between the k–ε and VLES turbulence closure models.

Table 2
Parameters of the stability functions

A_1	A_2	B_1	B_2	C_2	C_3	G_{h_min}	G_{h_0}	G_{h_crit}
0.92	0.74	16.6	10.1	0.7	0.2	−0.28	0.0233	0.02

4. Model setup and parameters

The topography in the model is derived from multi-beam echosounder data of the northern channel of Red Sea (Fig. 2) between Station 35 and Station 39. The positions of stations are shown in Fig. 3. The domain is 102 km long and has a maximum depth of 1.28 km. The flow is forced by observed temperature and salinity profiles at the inlet, the left boundary coinciding with the location of Station 35. There is also a net transport specified at the top boundary for the stream function. REDSOX-1 observations clearly show a surface mixed layer, which is approximately 100 m thick, salty and warm because of heating and evaporation. The surface mixed layer is important since it occupies a significant portion of the water depth. As this layer has nearly constant properties along the channel, it is used as part of initial condition and maintained by relaxation to the observed data (Fig. 7). A buffer zone is implemented downstream of Station 9 to absorb the incoming flow. This buffer zone is for salinity and temperature, while an Orlanski-type boundary condition (Orlanski, 1976) is used for vorticity.

The realistic Pr based on molecular values for heat is $Pr \approx 7$ and $Pr \approx 700$ for salt. The effect of such high Pr is to extend active tracer cascade to smaller spatial scales beyond the dissipation scale of momentum. As such, active tracers tend to exhibit thinner boundary layers, which can lead to various interesting phenomena at small scales, such as Hölmböe shear instability (Hölmböe, 1962) or double-diffusive instability (Stern, 1960). The resolution of such small-scale instabilities as well as development of appropriate SGS models is beyond the the scope of the present study. Their consideration would particularly violate our overall VLES philosophy which implicitely rests on very high *local* Reynolds numbers which thus implies $Pr = 1$ for all scalars. The Froude number $Fr = U_0/Nh_0 = U_0/\sqrt{g\Delta\rho' h_0/\rho_0}$ is set as follows. The velocity scale is assumed as that of the initial gravity current speed, $U_0 = \sqrt{g\Delta\rho' h/\rho_0}$. Also, initially $h_0 = 2h$ since h_0 is the initial depth at the inlet of model. Therefore, the Froude number is set to $Fr = 1/\sqrt{2}$, and this value is in the range of observations from Peters et al. (2005b). Using a thermal expansion coefficient of $\alpha = 1.7 \times 10^{-4}\ ^\circ\mathrm{C}^{-1}$ and saline contraction coefficient $\beta = 7.5 \times 10^{-4}\ \mathrm{psu}^{-1}$ estimated in the temperature range of 14.5–25.5 °C and the salinity range of 35.6–39.9 psu, the density ratio is set to 0.579.

Insulated (zero flux) boundary conditions are applied for salinity and temperature at the bottom and top surface (i.e. $\partial S/\partial \mathbf{n} = \partial T/\partial \mathbf{n} = 0$, where $\mathbf{n}$ is normal to the surface). A net transport is also specified as $\psi_{\mathrm{net}} = 105\ \mathrm{m}^2\ \mathrm{s}^{-1}$ at the top surface; detailed information can be found in Özgökmen et al. (2003). A free-slip boundary condition is applied for the top surface. For the bottom boundary, wall-layer condition is applied to vorticity, in that

$$\zeta = -\frac{\partial u}{\partial z} + \underbrace{\frac{\partial w}{\partial x}}_{0} \text{ at } z = z_{\mathrm{bottom}} \tag{20}$$

$$\tau_{\mathrm{bottom}} = \nu \frac{\partial u}{\partial z} = C_{\mathrm{d}} U|U|, \tag{21}$$

where C_{d} is the drag coefficient which is governed by the vertical mesh size and the length of the bottom-roughness elements (Baumert and Radach, 1992). τ_{bottom} is the shear at the bottom. From (20) and (21), we get the nondimensional form of the vorticity boundary condition at the bottom,

$$\zeta_{\mathrm{bottom}} = -Re_t \cdot C_{\mathrm{d}} U|U|, \tag{22}$$

where U is taken at the first grid point ($\Delta z/2$).

The boundary conditions for k and ε at the bottom are obtained by assuming a local balance between production and dissipation from Eq. (5), namely $P = \varepsilon$ (see Baumert and Radach, 1992; Burchard and Baumert, 1995 for details):

$$k = |U_{\mathrm{f}}|^2 c_\mu^{-1/2}, \tag{23}$$

$$\varepsilon = \frac{U_{\mathrm{f}}^3}{\kappa z}, \tag{24}$$

where $U_f = u_f/U_0$ is the nondimensional bottom friction velocity found from $U_f = \sqrt{C_d U^2}$ and the von Kármán constant $\kappa = 1/\sqrt{2\pi} \approx 0.399$.

Estimates of the bottom drag coefficient from overflow observations indicate a broad range of $1 \times 10^{-3} \leqslant C_d \leqslant 10 \times 10^{-3}$ (Girton and Sanford, 2003; Peters and Johns, 2006). Modeling of the drag coefficient for flows over irregular topography is a complex problem in its own right. Here, a single value of C_d is used for simplicity. In order to decide on this value, several experiments with different Reynolds numbers and resolutions are conducted. First, low resolution and low Reynolds number ($\Delta x \approx 200$ m, $\Delta z \approx 10$ m, $Re = 5000$) experiments have been conducted with three different drag coefficient values: $C_d = 1 \times 10^{-3}$, $C_d = 5 \times 10^{-3}$, and $C_d = 8 \times 10^{-3}$. The results are compared with data from REDSOX stations, which show that $C_d = 5 \times 10^{-3}$ and $C_d = 8 \times 10^{-3}$ achieve better results than $C_d = 1 \times 10^{-3}$ (Fig. 5). Then, both the Reynolds number and horizontal resolution are increased ($\Delta x \approx 100$ m, $\Delta z \approx 10$ m, $Re = 10^4$) to carry out further comparisons between these two under different circumstances. As shown in Fig. 6, $C_d = 5 \times 10^{-3}$ gives somewhat better results than $C_d = 8 \times 10^{-3}$, and therefore $C_d = 5 \times 10^{-3}$ is used in all the following experiments.

The model parameters are summarized in Table 3.

The experiments are conducted on a Linux server with four AMD dual-core Opteron 865 processors (1.8 GHz) and 16 GB of RAM. Two-dimensional simulations without SGS parameterizations at high resolution are conducted on four processors and take approximately one day in real time, whereas simulations with VLES and standard k–ε at high resolution take approximately five days on four processors. VLES and k–ε are more time consuming since the sink and source terms in the turbulence closure equations demand a smaller time step than in under-resolved DNS model to satisfy the Courant–Friedrich–Levy criterion. Experiments

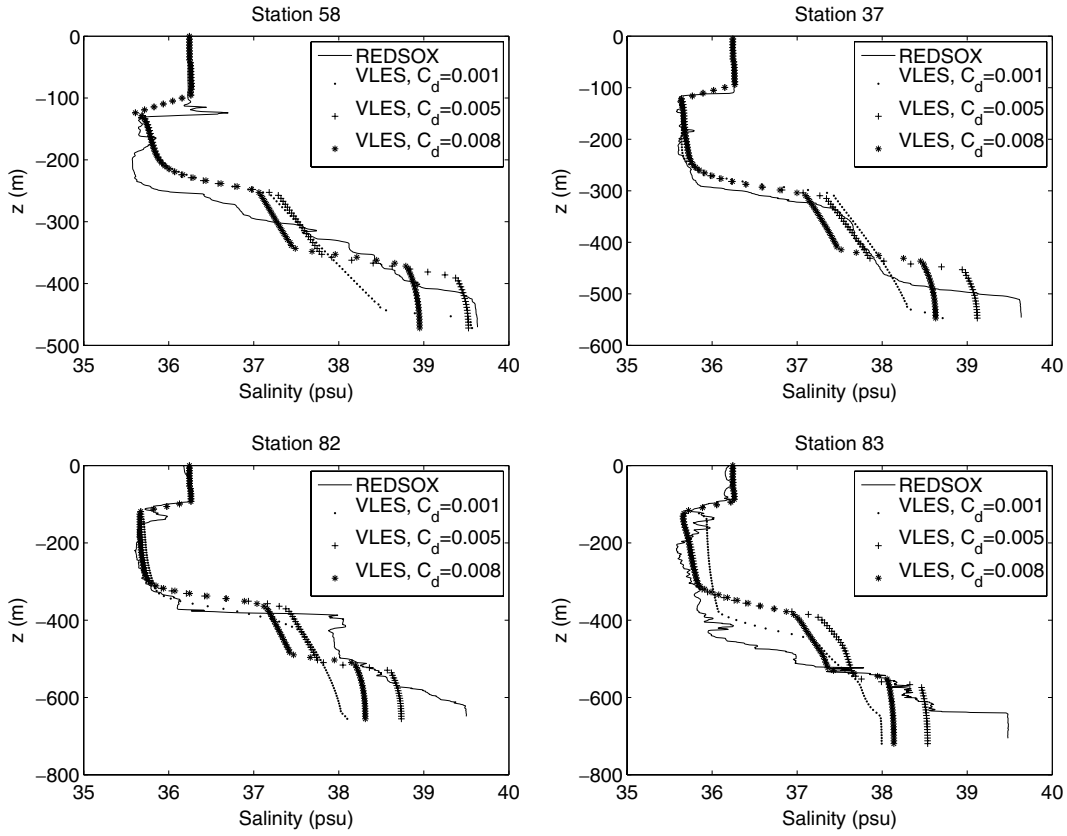

Fig. 5. Comparison of salinity profiles from REDSOX-1 stations 58, 37, 82 and 83 to those obtained with VLES using C_d values of 1×10^{-3} (dotted lines), 5×10^{-3} (lines with +), and 8×10^{-3} (lines with *) for $Re = 5000$, $\Delta x \approx 200$ m, $\Delta z \approx 10$ m.

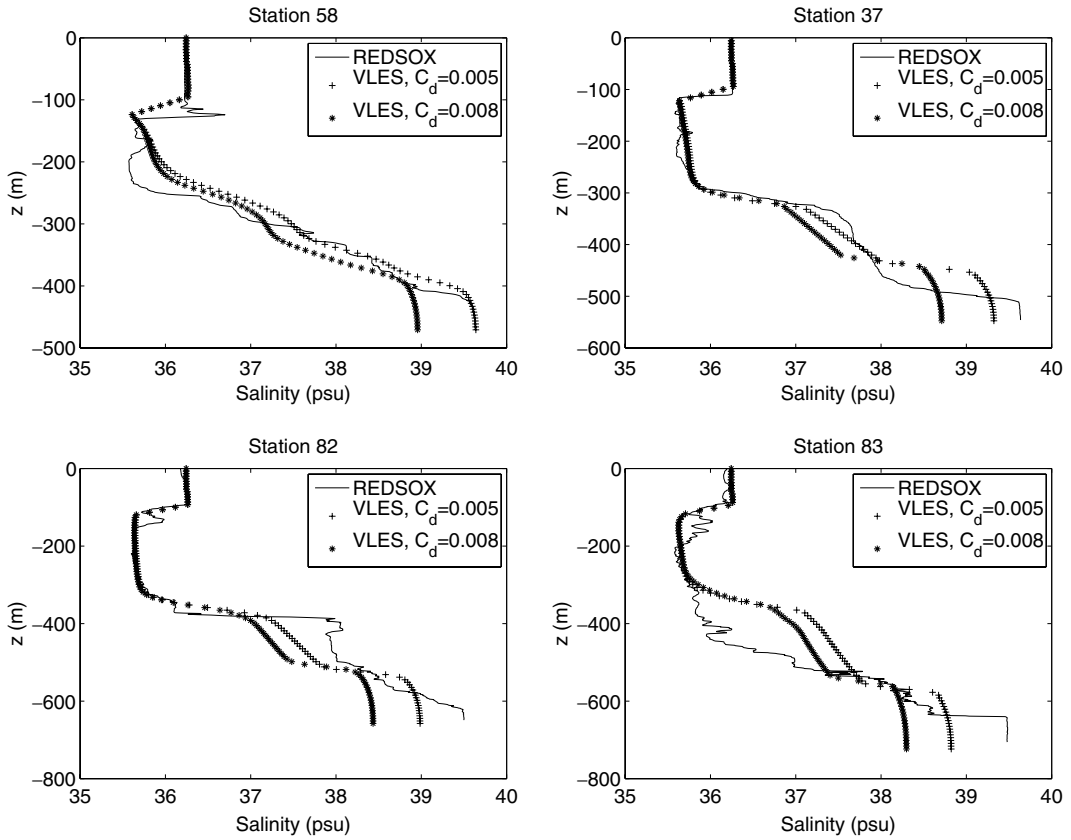

Fig. 6. Comparison of salinity profiles from REDSOX-1 stations 58, 37, 82 and 83 to those obtained with VLES using C_d values of 5×10^{-3} (lines with +) and 8×10^{-3} (lines with *) for $Re = 10,000$, $\Delta x \approx 100$ m, $\Delta z \approx 10$ m.

Table 3
Parameters of the numerical simulation

L_x	H	Fr	R_ρ	Pr	C_d	ψ_{net}
102 km	1.28 km	0.707	0.579	1	5×10^{-3}	105 m^2/s

with resolutions better than $\Delta x = 50$ m and $\Delta z = 10$ m have not been performed because of their computational expense.

5. List of experiments and evaluation strategy

The main experimental matrix consist of 30 cases, with three different models, at three Reynolds numbers, and three different horizontal resolutions, and two different vertical resolutions (Table 4). The models are standard k–ε, VLES and one without SGS stresses (or under-resolved 2D DNS). The latter is important is understand whether turbulence models are necessarily needed in the simulations. The main task is to explore which set of model equations leads to the best agreement with REDSOX-1 observations. It is also important to investigate the dependence of the results on Re. This is because oceanic Re is extremely high. If results from k–ε or VLES change with Re, this will obviously pose some questions regarding the utility of these approaches for oceanic overflow simulations. Finally, resolution dependence is explored. The k–ε model presumably parameterizes the effect of all turbulence. As such, there is no information about resolved scales in such models. On the other hand, VLES incorporates information about the model resolution via (16). The performance of these models in a nonhydrostatic setting must be explored.

Table 4
List of experiments, consisting of different turbulence closures, Reynolds numbers, horizontal and vertical resolutions

No SGS			VLES			k–ε		
Re	Δx (m)	Δz (m)	Re	Δx (m)	Δz (m)	Re	Δx (m)	Δz (m)
5000	200	10	5000	200	10	5000	200	10
5000	100	10	5000	100	10	5000	100	10
5000	50	10	5000	50	10	5000	50	10
10,000	200	10	10,000	200	10	10,000	200	10
10,000	100	10	10,000	100	10	10,000	100	10
10,000	50	10	10,000	50	10	10,000	50	10
20,000	200	10	20,000	200	10	20,000	200	10
20,000	100	10	20,000	100	10	20,000	100	10
20,000	50	10	20,000	50	10	20,000	50	10
20,000	200	20	20,000	200	20	20,000	200	20

In order to assess whether the model spatial resolutions employed here (Table 4) are adequate to take advantage of the VLES filtering procedure (16), the following simple estimate is provided. In a stratified flow, the length scale of the energy containing eddies is expected to be in the range of $\ell_O < L < \ell_d$, where $\ell_O = \sqrt{\epsilon/N^3}$ is the Ozmidov scale and $\ell_d = (\nu^3/\epsilon)^{1/4}$ is the Kolmogorov length scale. In the limit of $\delta < \ell_d$, all turbulence is resolved, and the computations correspond to DNS. In the limit of $\delta > \ell_O$, the method is equivalent to the k–ε turbulence closure. In gravity currents, one can expect $\ell_O \approx 0.4\, h_0$, where h_0 is the overflow thickness (Eq. (40) in Özgökmen et al., 2007). The typical overflow thickness is $h_0 \approx 300$ m in the present case, thus one would expect an upper limit for the overturns as $\ell_O \approx 120$ m. For the finest resolution cases with $\Delta x = 50$ m and $\Delta z = 5$ m, $\delta = 32$ m from (17), which indicates that the overturns would be well resolved. For the coarsest resolution case with $\Delta x = 200$ m and $\Delta z = 20$ m, (17) yields $\delta = 126$ m, which could be classified as eddy-permitting. Note that in the actual computations, L is not constant but obtained from the local dynamical estimate (15), which may allow the VLES to respond to intermittent turbulence. The above a priori estimates imply that $\delta \leqslant L$, namely the model resolution is near the top of the eddy break down and energy cascade process, and we expect the VLES results to differ with respect to those using the k–ε turbulence closure.

Two different approaches can be followed in evaluating the performance of turbulence closure models (Sagaut, 2005). The first may be called *a priori* approach, in which the turbulent kinetic energy k and its dissipation rate ε are *directly* compared to measurements. An example of this approach can be found in the recent study by Peters and Baumert (2007). This approach requires the availability of proper turbulence observations which are quite rare and which are often incomplete as either only the dissipation rate is measured or only the Thorpe scale or the Reynolds stress are available. Generally, this approach rests on measurement of second moments of the hydro-thermodynamic fields.

The second approach may be called *a posteriori* method and aims at an indirect evaluation using only first moments of the state variables for comparison observations, namely simply the water temperature or current or salinity or even quantities of still higher integrative character like the mass or volume transport through certain cross sections.

In this study, we conduct *a posteriori* testing, by comparing modeled salinity, temperature and velocity profiles and overflow mass transport to those from REDSOX-1 observations.

6. Results

6.1. Description

Snapshots of the salinity distribution from the high resolution-high Re number ($\Delta x = 50$ m and $Re = 20{,}000$, henceforth HighRe) experiments are plotted in Fig. 7 to describe the time evolution of the outflow. The formation of a characteristic head is observed in the case without SGS parameterization. This is a transient feature associated with the initial propagation and does not carry much significance for overflows in

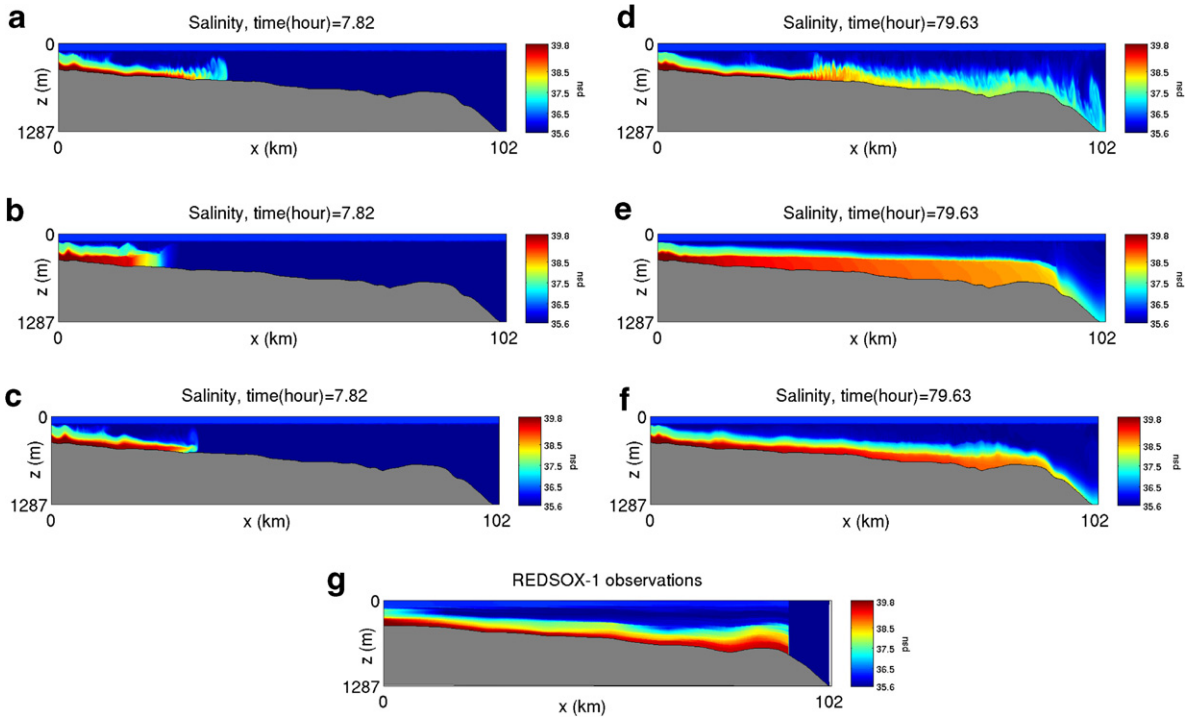

Fig. 7. Salinity distribution of the HighRe model with w/out SGS ((a) and (d)), standard k–ε ((b) and (e)) schemes, VLES ((c) and (f)), respectively as a function of time at $t = 7.82$ h ((a)–(c)) and $t = 79.63$ h ((d)–(e)). (g) The salinity distribution based on REDSOX-1 observations is plotted in (g). Animations are available from: http://www.rsmas.miami.edu/personal/milicak/2dnonhydrostaticmodel.html.

statistical equilibrium. The overflow travels over the channel's topography and reaches the western boundary after 31.7 h ($\approx$ 1.3 days). Further integration shows the emergence of a hydraulic-jump like transition approximately 30 km into the domain (Fig. 7d). This transition coincides with the increase in the slope angle, and appears to result in a significant dilution of the overflow, removing the distinction between the IL and BL seen in the observations. Such high mixing as in Fig. 7d appears to be inconsistent with the REDSOX-1 observations. As such, we conclude that one of the key requirements for the turbulence closures is to impact the solution such that the distinction between IL and BL is preserved.

Salinity snapshots from experiments with the same resolutions and Reynolds numbers (HighRe case) but with turbulence closures k–ε and VLES are plotted in Fig. 7 as well. Both k–ε and VLES satisfy the above requirement, namely they result in distinct IL and BL in the overflow. While the characteristics of results from k–ε and VLES are similar qualitatively, they differ quantitatively. For instance, the overflow in the equilibrium state in VLES (Fig. 7f) is characterized by a layer at the bottom approximately 100 m thick, which is well mixed and transports the dense water signal along the channel with little dilution. Above this bottom layer, there is another layer approximately 200 m thick where temperature and salinity values gradually decreases away from the bottom due to mixing with ambient water masses. The realism of these solutions can be assessed using the salinity distribution from REDSOX-1 observations, illustrated in Fig. 7g. The REDSOX-1 salinity field is plotted by interpolating the data between the stations. Observed fields are not shown after Station 9 since that region coincides with the model's radiation boundary condition zone, therefore model fields do not reflect the underlying physics in that regime. The results from VLES appear to show a better agreement with the observations than that from k–ε. In particular, the k–ε model seems to result in unrealistic thicknesses for both BL and IL. The dramatic change in the flow pattern from the case without SGS, and those with turbulence closures appears to be related to the turbulent Prandtl number (Pr_t). The stability functions play important roles to calculate the Pr_t (see the Eq. (10)). When Pr_t is set equal to 1 explicitly, k–ε

models produce very similar results to the model without SGS (not shown in here). More quantitative and extensive model-data comparisons at individual stations follow next.

6.2. Comparison of modeled and observed salinity and temperature profiles

The temperature and salinity profiles are compared with the REDSOX-1 observations along the northern channel. Four stations along the northern channel (Fig. 3) are chosen to compare the vertical structure of the plume. The salinity and temperature profiles are compared for the LowRe case in Figs. 8 and 9, respectively, and also for the HighRe case in Figs. 10 and 11. In these figures, data collected in the REDSOX-1 cruise are compared with time mean of the computed profiles. Time averaged salinity and temperature fields are calculated from $\overline{X} = (\tau_2 - \tau_1)^{-1} \int_{\tau_1}^{\tau_2} X \, dt$, where the time interval is chosen as $\tau_1 = 1.3$ days and $\tau_2 = 4.3$ days , which corresponds to the period after the modeled outflows reach a quasi-steady state. In order to show the variability of the profiles during this time period, 95% confidence intervals are also shown around the mean profiles. The behavior of the temperature with different models (Figs. 9 and 11) is similar to that of the salinity (Figs. 8 and 10). Thus, the following comparisons and discussions are based on salinity profiles.

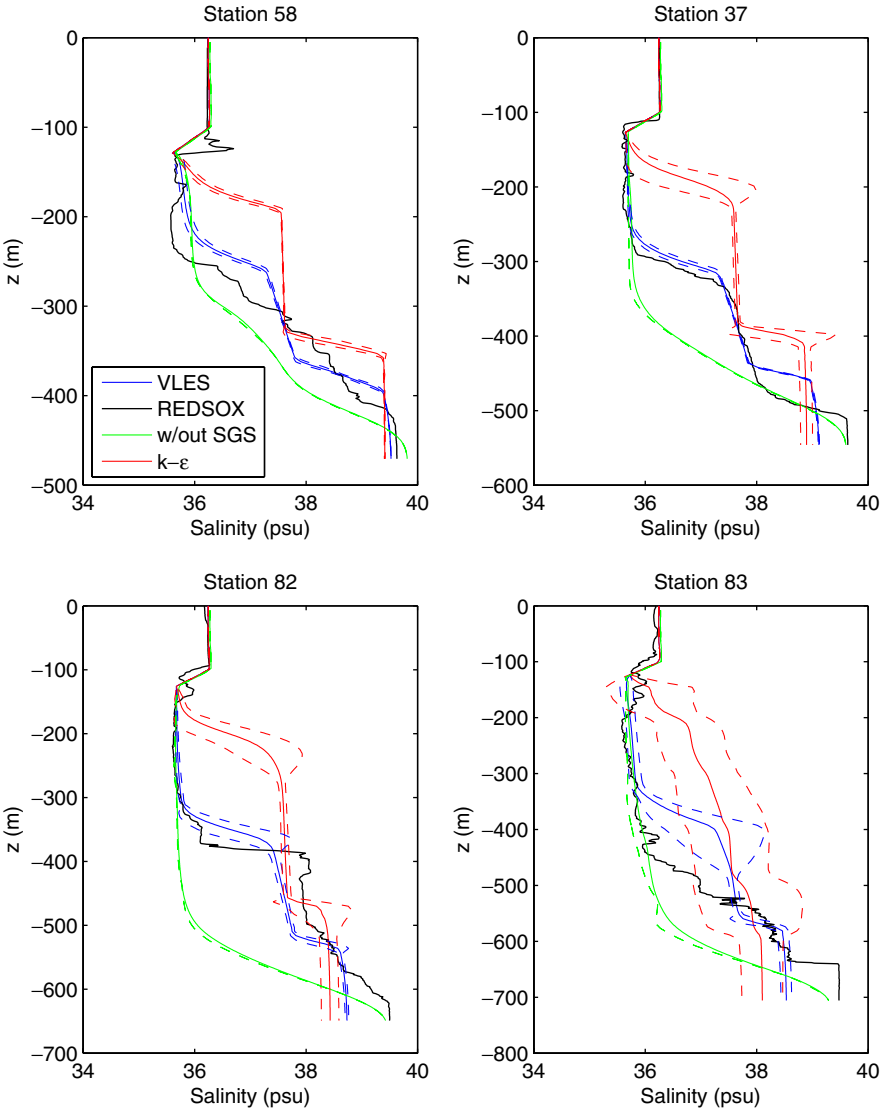

Fig. 8. Comparison of the salinity profiles for LowRe case. Dashed lines represent variability of the means with 95% confidence.

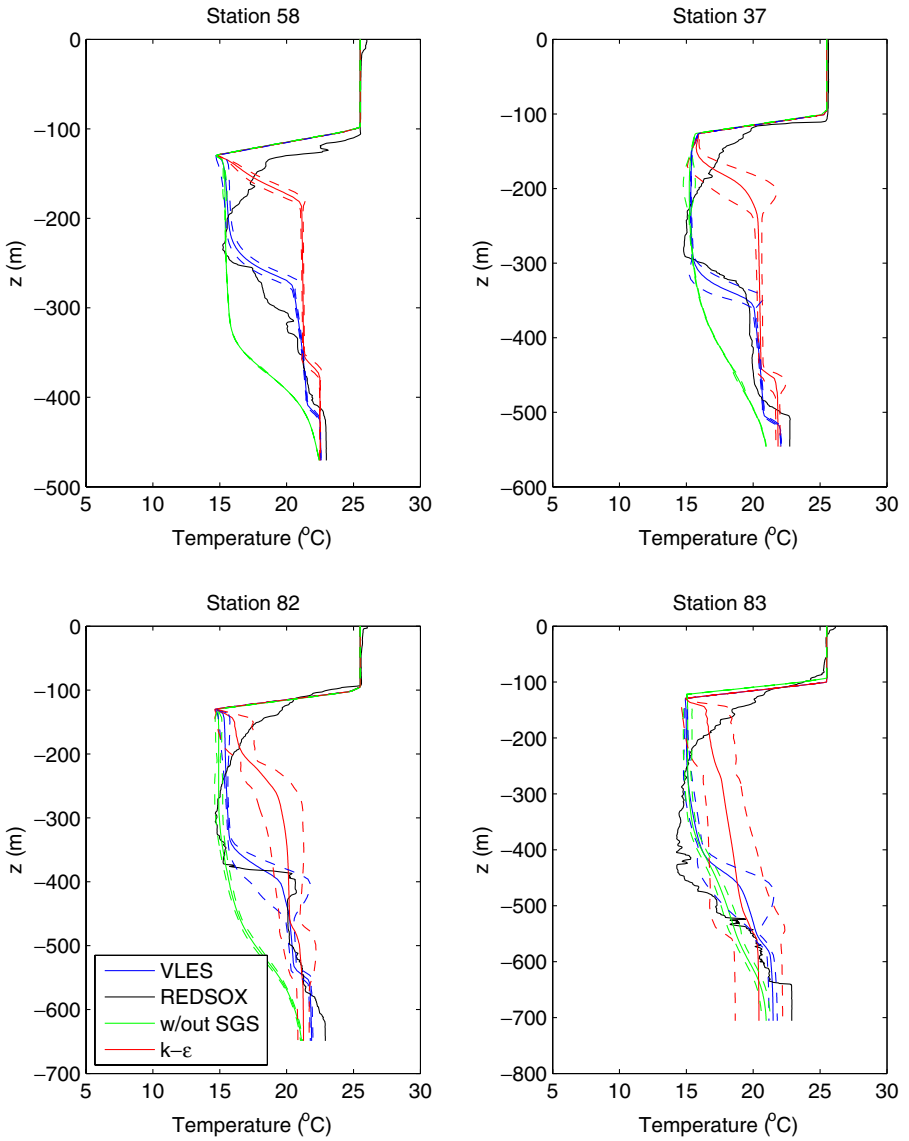

Fig. 9. Comparison of the temperature profiles for LowRe case. Dashed lines represent variability of the means with 95% confidence.

When the model is run without any SGS parameterization, results are not satisfactory because of excessive mixing and variability, and it is really hard to achieve even a quasi-steady solution. For LowRe, mixing is not enough and there is formation of an IL (green[1] curve in Fig. 8), while for HighRe there is adequate mixing to form an IL, however the BL is dramatically decreased (green[2] curve in Fig. 10), and outflow signal becomes weak. In the standard k–ε, the IL is thicker than observed, especially in LowRe case. One of the limitations of k–ε models is that they are designed for flows with steady mean flows. As such, this transient problem could be tough to handle. This may help explain the resulting high diffusivities, and a thicker IL (red curves in Figs. 8 and 10). The BL is also thicker than the observational data. As such, the k–ε model appears to cause overly thick BL and IL. Finally, the variability of the profiles around the mean is also quite high with the k–ε model. Salinity profiles obtained using VLES show the most faithful agreement with observations (blue curves in

[1] For interpretation to color in Fig. 8, the reader is referred to the web version of this article.
[2] For interpretation to color in Fig. 10, the reader is referred to the web version of this article.

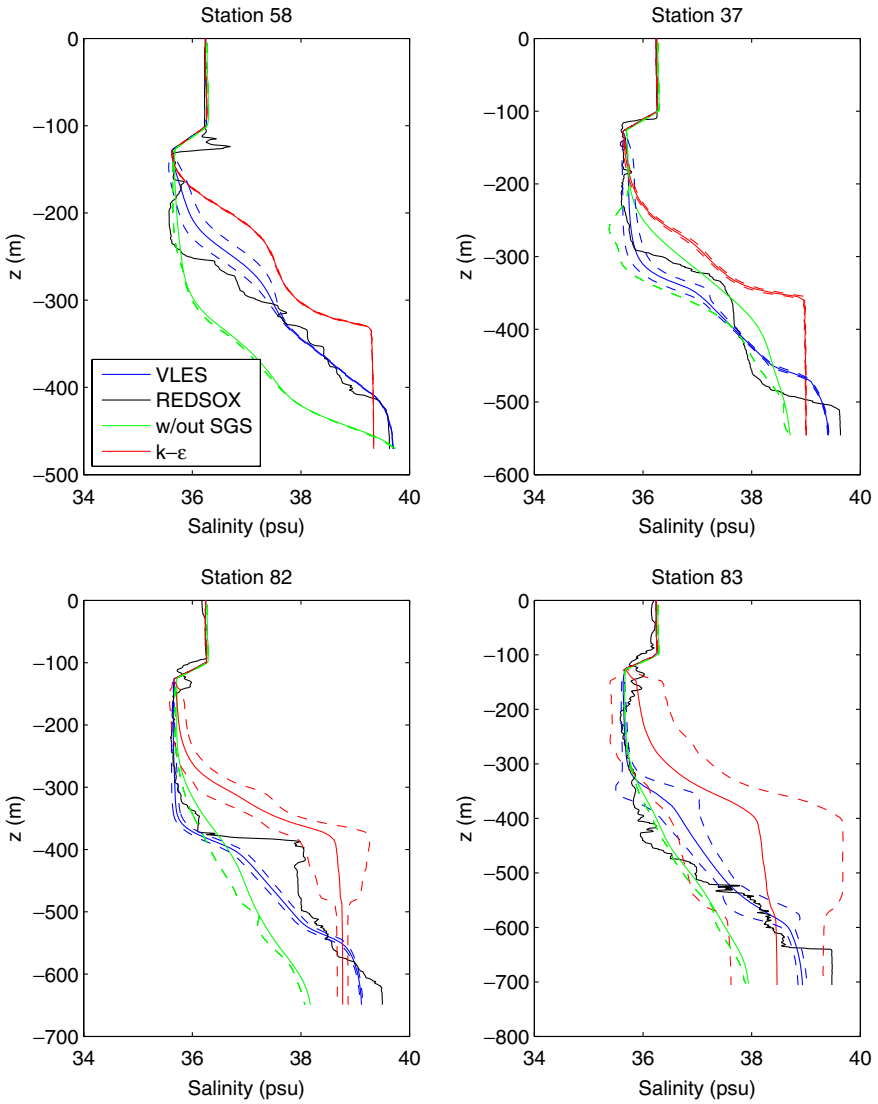

Fig. 10. Comparison of the salinity profiles for HighRe case. Dashed lines represent variability of the means with 95% confidence.

Figs. 8 and 10). Even in low Reynolds number – low resolution configuration, results are quite promising. High salinity and temperature signals at the bottom layer advected throughout the channel with little dilution, both the BL and IL are consistent with the REDSOX-1 observations.

6.3. Sensitivity to grid spacing

Different horizontal resolutions are used to examine the grid sensitivity of the three different models. For the lowest resolution $\Delta x = 200$ m and $\Delta z = 10$ m, and for mid-resolution $\Delta x = 100$ m and $\Delta z = 10$ m are used. The finest resolution is $\Delta x = 50$ m and $\Delta z = 10$ m. For most of the experiments, the vertical resolution is 10 m, since according to Peters and Johns (2006), the average bottom layer is 100 m thick, thus an adequate numner of grid points has been used to capture this layer. Salinity comparisons at different resolutions for $Re = 20{,}000$ are plotted in Fig. 12. The first impression from this figure is that increasing the resolution gives better results for VLES and k–ε.

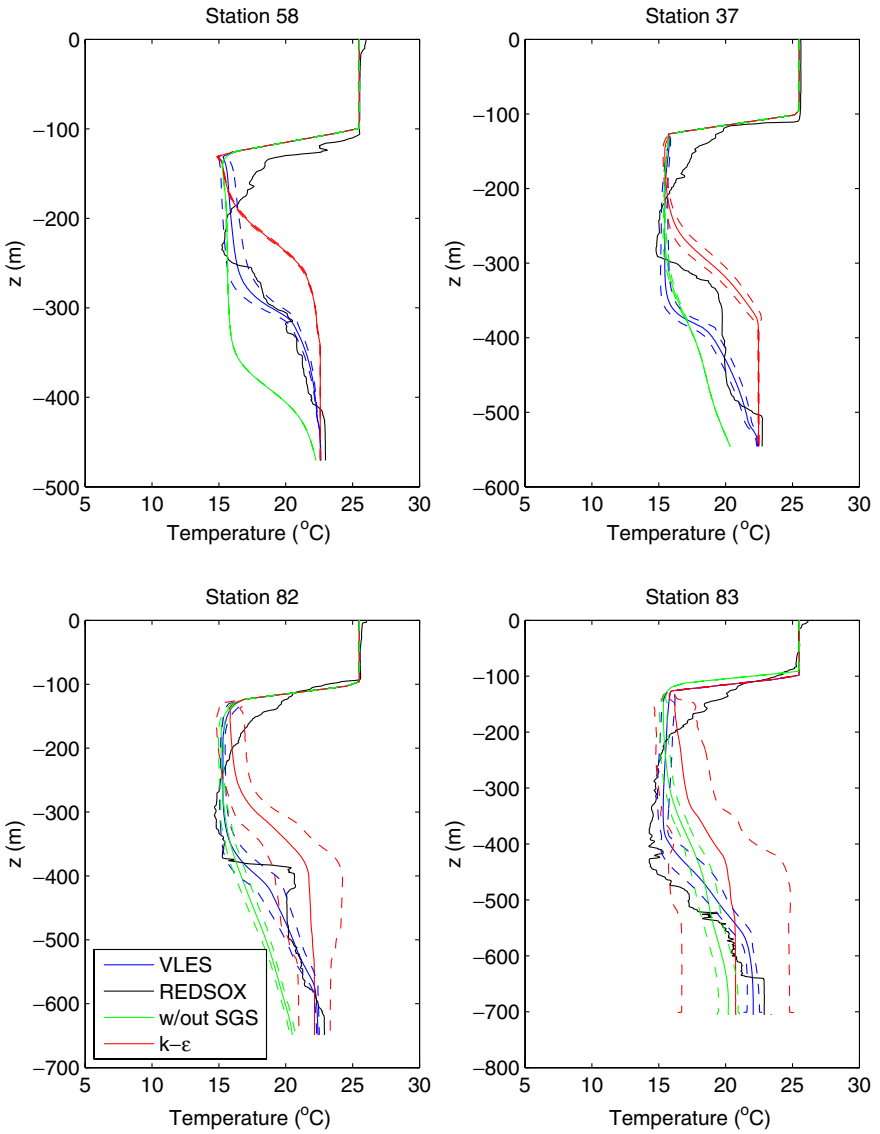

Fig. 11. Comparison of the temperature profiles for HighRe case. Dashed lines represent variability of the means with 95% confidence.

In order to quantify the difference between the results of the different resolutions of the different models, an error function is defined as

$$\mathrm{Error}_S \equiv \frac{1}{n}\sum_{i=1}^{i=n}\frac{1}{\Delta S r}\sqrt{\sum_{j=1}^{j=N^i}\left[\overline{S}^i_{\mathrm{model}}(j) - S^i_{\mathrm{obs}}(j)\right]^2/N^i}, \tag{25}$$

where $\overline{S}^i_{\mathrm{model}}$ is time-averaged model output, and S^i_{obs} is REDSOX-1 data at station i, N^i is the number vertical sampling points at each data station, n is the number of stations, Error_S is the root mean square (rms) error normalized by salinity range $\Delta S = 3.5$ psu and averaged over selected stations. Only observations within the overflow plume, defined by a salinity interface larger than 36.5 psu, are used to compute the error. Using four stations, namely 58, 37, 82 and 83, the average Error_S is computed for different closures, and plotted as a function of the horizontal resolution in Fig. 13 for the cases with $Re = 20{,}000$. It can be seen that the most consistent model is VLES, since error (%) is lowest and nearly resolution-independent (decreases slightly with

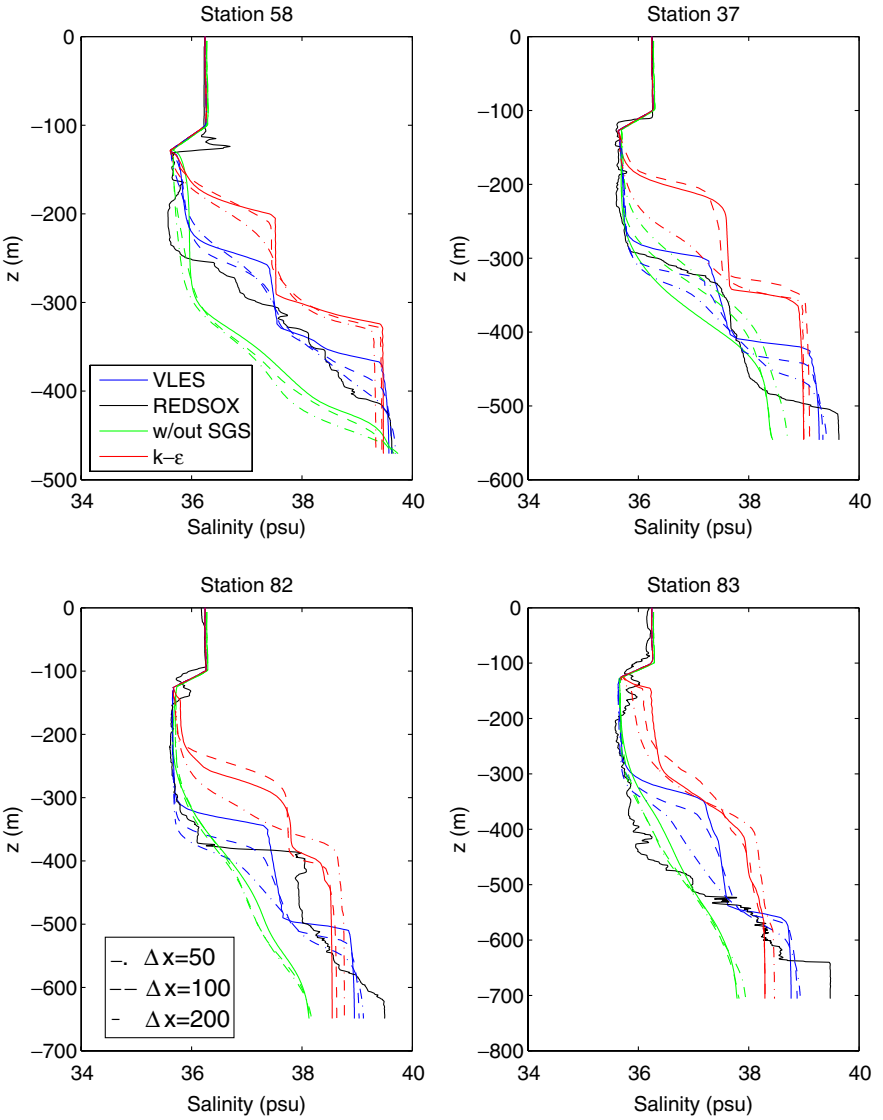

Fig. 12. Comparison of the salinity profiles for $Re = 20{,}000$. Solid lines, dashed lines, and dotted-dashed lines indicate resolutions of $\Delta x = 200$ m and $\Delta z = 10$ m, $\Delta x = 100$ m and $\Delta z = 10$ m, and $\Delta x = 50$ m and $\Delta z = 10$ m, respectively.

increasing resolution). The average error of VLES is around 10%, and it has a very similar profile (structure of IL and BL) compared to the real data. However, average errors in both k–ε, and without SGS are quite high (around 20%); the former overshoots the real data, and the latter underestimates it. The error is quite low at low resolution in the model without SGS parameterization, when none of the flow turbulence is resolved and the model fields are basically laminar. The net effect of this is to transport to some extent the basic inflow structure consisting of a BL and an IL. When the resolution is increased, the model starts to capture finer turbulent structures, yet these structures appear to destroy the overflow structure. Presumably, in the case of DNS, all the turbulent effects will be captured in a way to restore the BL and IL, but we appear to be very far away from such a simulation without a closure model. Errors for temperature (not shown in here) are very similar to the errors for salinity, and this appears to confirm the model consistency. In order to quantify how errors change with Re, they are also plotted for $Re = 10{,}000$ in Fig. 13. It should be mentioned here that two-equation turbulence closures are theoretically designed for very high Reynolds number. As such, when the

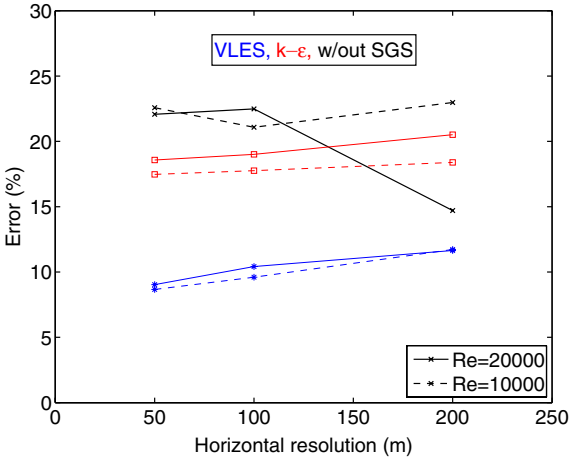

Fig. 13. Averages of normalized salinity errors (%) of the stations, errors are computed between three different models with three different horizontal resolutions and REDSOX-1 observations for $Re = 20{,}000$ (solid lines) and $Re = 10{,}000$ (dashed lines).

Reynolds number is increased from 10,000 to 20,000, errors from standard k–ε and VLES change only by a few percent, on average. This also shows the consistency of the models.

The dependence of the model performances on the vertical grid spacing is also investigated. In Fig. 14, results from different vertical resolutions are plotted with $\Delta x = 200$ m and $Re = 20{,}000$. The boundary layer becomes very weak and strongly diluted in the case without a SGS model, when the vertical resolution is decreased (dashed green[3] lines in Fig. 14). The performance of the k–ε model does not seem to change much with different vertical resolutions (see the red lines of Stations 58, 82, and 83). In VLES, high resolution case gives better results only in Stations 37, and 82. However, differences among stations are not significant for different vertical resolutions. Therefore, we conclude that k–ε and VLES models are fairly insensitive to the vertical resolution when the overflow is adequately resolved, that is for $\Delta z = 10$ m and $\Delta z = 20$ m corresponding to 15–30 points in the overflow layer. We did not try a coarser mesh, such as $\Delta z = 40$ m, since the oceanic BL is approximately 100–150 m thick, and trying to represent it with only three grid points is not likely to be fruitful.

6.4. Comparison of modeled and observed velocity and mass transport

A comparison of the modeled and observed velocity distributions at selected stations along the northern channel are depicted in Fig. 15. As in temperature and velocity profiles, VLES results in the best fit with data. In particular, the maximum velocity coincides with the starting point of the IL, and its depth and magnitude are comparable with REDSOX-1 data. In k–ε model, the location of the velocity maximum is too far up in the water column and the ambient fluid speed is too high, whereas the case without an SGS model leads to a thinner and faster overflow than observed. One of the striking features is that there is a significant reduction in the overflow speed from REDSOX-1 data at station 37. This raises the issue of sampling and synopticity in the velocity field compared to tracer field in the observations. A good illustration of the concept that the velocity field may be more variable than the tracer fields is given in Fig. 9 of Peters et al. (2005b).

The normalized mass transport, $(Q(x) - Q_{\text{in}})/Q_{\text{in}}$, is calculated from both the HighRe cases and REDSOX-1 velocity data, where $Q(x)$ is the transport of the outflow as a function of downslope distance x, $(Q(x) = \int u(x)\mathrm{d}z)$, and Q_{in} is the outflow transport at the inlet (Station 35). To estimate the $Q(x)$ from the model, the mean transport of stream function, $\bar{\psi}$, is calculated during the equilibrium phase $1.3 \leqslant t \leqslant 4.3$ days. The results plotted in Fig. 16 show a few striking features. The first is that in all models the transport remains nearly constant until 35–40 km down the slope, and then starts increasing, albeit at dif-

[3] For interpretation to color in Fig. 14, the reader is referred to the web version of this article.

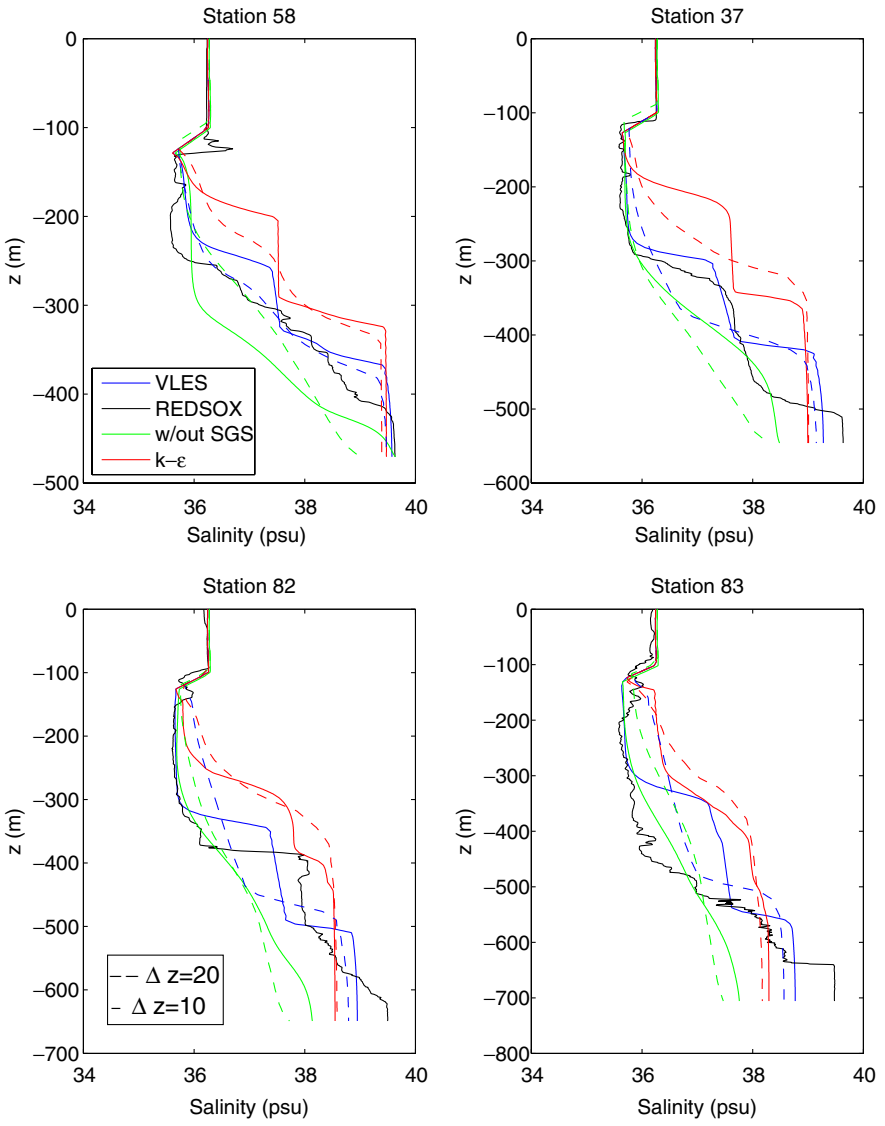

Fig. 14. Comparison of the salinity profiles for $Re = 20{,}000$. Solid lines, dashed lines, indicate resolutions of $\Delta x = 200$ m and $\Delta z = 10$ m, $\Delta x = 200$ m and $\Delta z = 20$ m, respectively.

ferent rates depending on the model, presumably because of the increasing slope angle. The case without an SGS model shows the most dramatic increase in transport, doubling by the end of the model domain, which is consistent with the excessive mixing seen in Fig. 7d. The k–ε model leads to the smallest amount of transport, but exhibits a spike at the very end of the channel. Experiment with VLES illustrates an overflow transport that is larger than those with k–ε, but still significantly smaller than the case without an SGS model. The transport increase of the plume is approximately 80% along the channel in VLES case. This is in good agreement with (Özgökmen et al., 2003), see the Fig. 14 from that paper. Transports based on REDSOX-1 data raise some questions. While the estimate at Station 58 is in excellent agreement in all cases, the REDSOX-1 transport drops significantly after about 20 km downstream at Station 37. We believe that this is likely to a sampling issue, such as synoptic variability and/or reliance on integration of one-dimensional profiles for estimating the overflow transport. As such, it remains unclear to what extent the REDSOX-1 velocity observations provide a precise reference truth for differentiating the relative performance of these turbulence clo-

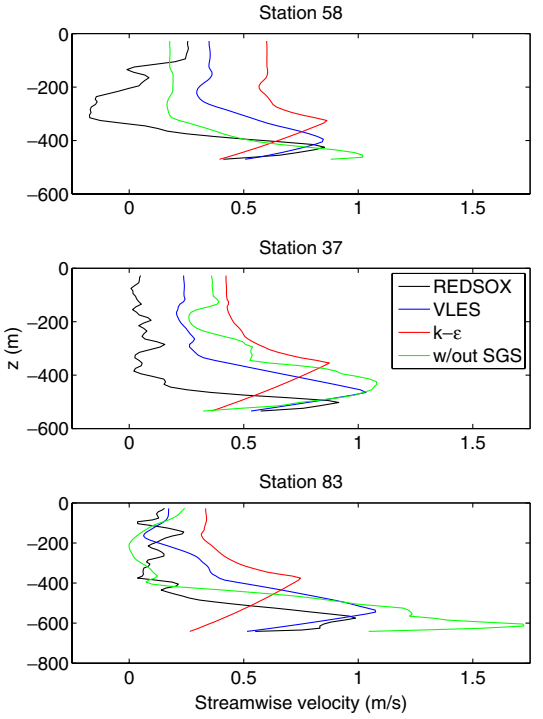

Fig. 15. Comparison of streamwise velocity profiles between three models with $Re = 20{,}000$ and REDSOX-1 observed data.

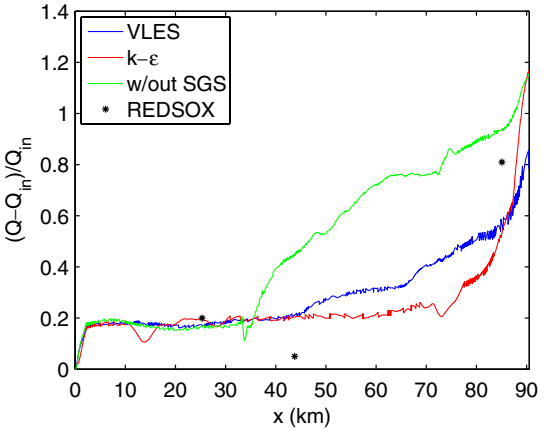

Fig. 16. Nondimensional net overflow transport as a function of downstream distance along the channel for $Re = 20{,}000$. Transports estimated from REDSOX-1 stations 58, 37, and 83 are marked by $(*)$.

sures. The overflow transport from observations appears to significantly increase at Station 83, and arrives within the range of model estimates.

7. Summary and conclusions

The development of parameterizations of overflow mixing is important not only for exploring the large-scale impacts of overflows in climate studies, but also for a better understanding of overflow dynamics in regional studies. Thus far, only simple algebraic mixing models have been validated using output from LES

studies and observational data. While the LES approach offers a reliable avenue to simulate the mixing, it is still computationally expensive for regional simulations of overflows.

The main objective of this study is to extensively test the performance of a comprehensive class of parameterizations, namely two-equation turbulence closures, or specifically k–ε models, for overflow simulations in a nonhydrostatic model. The k–ε models have a long history of development both in the engineering and oceanographic communities, but to our knowledge, they have not yet been tested using ground truth from overflow observations. Temperature and salinity observations from REDSOX-1 cruise provide valuable data to assess their performance. We focus on the main channel of overflow transport, which is not only narrow enough to allow the use of a 2D numerical model, but also the overflow characteristics here have been studied and identified from observations. Most strikingly, the overflow has a BL, which transports high salinity and temperature classes along the bottom nearly undiluted along the entire channel length, and an IL, where most of the shear, mixing and entrainment takes place. To have the distinction between BL and IL, and to capture their correct proportions and property distributions are the main challenges for the turbulence closure.

In this study, we put forward another approach as well. With the increase of computer power, it is inevitable that the resolution of coastal and ocean models will approach a range in which nonhydrostatic effects become important. Simultaneously, LES models will also expand their range of applications. While the Reynolds number in the ocean is high enough to prohibit the simultaneous resolution of all scales of motion, one still has to envision a range of applications in which turbulent coherent structures such as stratified overturns and dispersive internal waves are at least marginally resolved using nonhydrostatic models. As such, the question arises what the most appropriate SGS models for such models are, or in particular, whether one can adopt k–ε turbulence closures to be used in nonhydrostatic models. This can be done by applying a spatial filter to the k–ε equations, which allows the effect of this parameterization to vary depending on the range of resolved turbulence with the main fluid model. This is the main concept behind VLES, and to our knowledge, this is the first time that VLES is tested for an oceanographic application here.

A large set of experiments are conducted using not only k–ε and VLES but also without using any SGS model, which is important to assess the importance of the turbulence closure terms. Sensitivity of the results to Re and model resolution are also explored.

The comparison of modeled and observed salinity and temperature distributions yields the following conclusions. It is found that the experiments without SGS models cannot reproduce the basic structure of the northern channel overflow, because of excessive mixing throughout the overflow. As such, turbulence closures appear to be a necessity. The k–ε model yields unrealistically thick BL and IL, while VLES gets things just about right. The primary reason appears to be that RANS-type closure models parameterize all the turbulence, while nonhydrostatic models can resolve some part of the turbulence given adequate resolution. Thus, the combination of k–ε with nonhydrostatic dynamics appears to provide excessive mixing, namely without the balancing of the contributions presented via VLES. VLES results are found to be fairly consistent within the ranges of $10{,}000 \leqslant Re \leqslant 20{,}000$, $50\ \text{m} \leqslant \Delta x \leqslant 200\ \text{m}$ and $10\ \text{m} \leqslant \Delta z \leqslant 20\ \text{m}$. Velocity data from REDSOX-1 is vertically integrated to estimate the overflow transport, but the apparent sampling problems in the velocity observations prohibit their use to further differentiate between the turbulence models.

In summary, we conclude that k–ε or other turbulence closures appear to provide a promising avenue for extending the range of applicability of LES approaches to ocean modeling, by providing comprehensive SGS models for stratified turbulence.

Acknowledgements

We are grateful for the support of National Science Foundation via grants OCE 0352047 and OCE 0620661. We thank Yeon Chang for providing the bottom topography, and Marcello G. Magaldi for his constructive criticism.

References

Arakawa, A., 1966. Computational design for long-term numerical integration of the equations of fluid motion: Two dimensional incompressible flow part i. J. Comput. Phys. 1, 119–143.

Baines, P.G., 2001. Mixing in flows down gentle slopes into stratified environments. J. Fluid Mech. 443, 237–270.
Baines, P.G., 2005. Mixing regimes for the flow of dense fluid down slopes into stratified environments. J. Fluid Mech. 538, 245–267.
Baringer, M.O., Price, J.F., 1997. Mixing and spreading of the mediterranean outflow. J. Phys. Oceanogr. 27, 1654–1677.
Baumert, H.Z., Peters, H., 2000. Second-moment closure and length scales for weakly stratified turbulent shear flows. J. Geophys. Res. 105, 6453–6468.
Baumert, H.Z., Peters, H., 2004. Turbulence closure, steady state, and collapse into waves. J. Phys. Oceanogr. 34, 505–512.
Baumert, H.Z., Radach, G., 1992. Hysteresis of turbulent kinetic energy in nonrotational tidal flows: a model study. J. Geophys. Res. 97 (March), 3669–3677.
Baumert, H.Z., Simpson, J., Sündermann, J., 2005. Marine Turbulence. Cambridge University Press, Cambridge, UK.
Beal, L.M., Ffield, A., Gordon, A.L., 2000. Spreading of Red Sea overflow waters in the indian ocean. J. Geophys. Res. 105, 8549–8564.
Bower, A.S., Fratantoni, D.M., Johns, W.E., Peters, H., 2002. Gulf of Aden eddies and their impact on Red Sea Water. Geophys. Res. Lett. 29 (Nov), 1–21.
Bower, A.S., Johns, W.E., Frantantoni, D.M., Peters, H., 2005. Equilibration and circulation of Red Sea outflow water in the western gulf of aden. J. Phys. Oceanogr. 35, 1963–1985.
Buntić Ogor, I., Gyllenram, W., Ohlberg, E., Nilsson, H., Ruprecht, A., 2006. An adaptive turbulence model for swirling flow. In: Conference on Turbulence and Interactions TI2006. Porquerolles, France.
Burchard, H., Baumert, H., 1995. On the performance of a mixed-layer model based on the k–ε turbulence closure. J. Geophys. Res. 100, 8523–8540.
Canuto, V.M., Howard, A., Cheng, Y., Dubovikov, M.S., 2001. Ocean turbulence. part i: One-point closure model momentum and heat vertical diffusivities. J. Phys. Oceanogr. 31, 1413–1426.
Cenedese, C., Whitehead, J.A., Ascarelli, T.A., Ohiwa, M., 2004. A dense current flowing down a sloping bottom in a rotating fluid. J. Phys. Oceanogr. 34, 188–203.
Chang, Y.S., Xu, X., Özgökmen, T.M., Chassignet, E.P., Peters, H., 2005. Comparison of gravity current mixing parameterizations and calibration using high-resolution 3d nonhydrostatic spectral element model. Ocean Modell. 10, 342–368.
Dickson, R.R., Gmitrowics, E.M., Watson, A.J., 1990. Deep water renewal in the northern north atlantic. Nature 344, 848–850.
Ellison, T.H., Turner, J.S., 1959. Turbulent entrainment in stratified flows. J. Fluid Mech. 6, 423–448.
Ezer, T., 2005. Entrainment, diapycnal mixing and transport in three-dimensional bottom gravity current simulations using the mellor-yamada turbulence scheme. Ocean Modell. 9, 151–168.
Ezer, T., 2006. Topographic influence on overflow dynamics: Idealized numerical simulations and the faroe bank channel overflow. J. Geophys. Res. 111 (Feb), 2002.
Ezer, T., Mellor, G., 2004. A generalized coordinate ocean model and comparison of the bottom boundary layer dynamics in terrain-following and in z-level grids. Ocean Modell. 6, 379–403.
Geyer, F., Østerhus, S., Hansen, B., Quadfasel, D., 2006. Observations of highly regular oscillations in the overflow plume downstream of the faroe bank channel. J. Geophys. Res. 111 (Dec), 12020.
Girton, J.B., Sanford, T.B., 2003. Descent and modification of the overflow plume in the denmark strait. J. Phys. Oceanogr. 33, 1351–1364.
Girton, J.B., Sanford, T.B., Käse, R.H., 2001. Synoptic sections of the denmark strait overflow. Geophys. Res. Lett. 28, 1619–1622.
Gordon, A.L., Zambianchi, E., Orsi, A., Visbeck, M., Giulivi, C.F., Whitworth, T., Spezie, G., 2004. Energetics plumes over the western ross sea continental slope. Geophys. Res. Lett. 31 (21) (Art. No. L21302).
Griffies, S.M., Bing, C., Bryan, F.O., Chassignet, E.P., Gerdes, R., Hasumi, H., Hirst, A., Treguier, A.M., Webb, D., 2000. Developments in ocean climate modelling. Ocean Modell. 2, 123–192.
Hallberg, R., 2000. Time integration of diapycnal diffusion and richardson number dependent mixing in isopycnal coordinate ocean models. Mon. Weather Rev. 128 (5), 1402–1419.
Hallworth, M.A., Huppert, H.E., Phillips, J.C., Sparks, S.J., 1996. Entrainment into two-dimensional and axisymmetric turbulent gravity currents. J. Fluid Mech. 308, 289–311.
Hölmböe, J., 1962. On the behavior of symmetric waves in stratified shear layers. Geophys. Publ. 24, 67–72.
Jungclaus, J.H., Mellor, G., 2000. A three-dimensional model study of the mediterranean outflow. J. Mar. Sys. 24, 41–66.
Kantha, L.H., Clayson, C.A., 1994. An improved mixed layer model for geophysical applications. J. Geophys. Res. 99, 25266–252355.
Killworth, P.D., 1977. Mixing on the Weddell sea continental slope. Deep-Sea Res. 24, 427–448.
Kolmogorov, A., 1942. Equations of turbulent motion of an incompressible fluid. Izv. Akad. Nauk. SSR Ser. Phys. 6, 56.
Large, W., Gent, P.R., 1999. Validation of vertical mixing in an equatorial ocean model using large eddy simulations and observations. J. Phys. Oceanogr. 29, 449–464.
Large, W.G., McWilliams, J.C., Doney, S.C., 1994. Oceanic vertical mixing: A review and a model with a nonlocal boundary layer parameterization. Rev. Geophys. 32, 363–403.
Magagnato, F., Gabi, M., 2002. A new turbulence model for unsteady flow fields in rotating machinery. Int. J. Rot. Mach. 8 (3), 175–183.
Matt, S., Johns, W.E., 2007. Transport and entrainment in the Red Sea outflow plume. J. Phys. Oceanogr. 37, 819–836.
Mauritzen, C., Price, J., Sanford, T., Torres, D., 2005. Circulation and mixing in faroese channels. Deep Sea Res. Part II 52, 883–913.
Mellor, G.L., Yamada, T., 1982. Development of a turbulence closure model for geophysical fluid problems. Rev. Geophys. 30, 851–875.
Morcos, S.A., 1970. Physical and chemical oceanography of the Red Sea. Oceanogr. Mar. Biol. Ann. 8, 73–202.
Murray, S.P., Johns, W., 1997. Direct observations of seasonal exchange through the Bab el Mandab Strait. Geophys. Res. Lett. 24 (November), 2557–2560.
Orlanski, I., 1976. A simple boundary condition for unbounded hyperbolic flows. J. Comput. Phys. 21, 251–269.

Özgökmen, T.M., Chassignet, E., 2002. Dynamics of two-dimensional turbulent bottom gravity currents. J. Phys. Oceanogr. 32, 1460–1478.

Özgökmen, T.M., Johns, W.E., Peters, H., Matt, S., 2003. Turbulent mixing in the Red Sea outflow plume from a high-resolution nonhydrostatic model. J. Phys. Oceanogr. 33, 1846–1869.

Özgökmen, T.M., Fischer, P.F., Duan, J., Iliescu, T., 2004a. Entrainment in bottom gravity currents over complex topography from three-dimensional nonhydrostatic simulations. Geophys. Res. Lett. 31 (July), 13212.

Özgökmen, T.M., Fischer, P.F., Duan, J., Iliescu, T., 2004b. Three-dimensional turbulent bottom density currents from a high-order nonhydrostatic spectral element model. J. Phys. Oceanogr., 34.

Özgökmen, T.M., Fischer, P.F., Johns, W.E., 2006. Product water mass formation by turbulent density currents from a high-order nonhydrostatic spectral element model. Ocean Modell. 12, 237–267.

Özgökmen, T.M., Iliescu, T., Fischer, P.F., Srinivasan, A., Duan, J., 2007. Large eddy simulation of stratified mixing in two-dimensional dam-break problem in a rectangular enclosed domain. Ocean Modell. 16, 106–140.

Peters, H., Baumert, H.Z., 2007. Validating a turbulence closure against estuarine microstructure measurements. Ocean Modell. 19, 183–203.

Peters, H., Johns, W.E., 2005. Mixing and entrainment in the Red Sea outflow plume. part ii: Turbulence characteristics. J. Phys. Oceanogr. 35, 584–600.

Peters, H., Johns, W.E., 2006. Bottom layer turbulence in the Red Sea outflow plume. J. Phys. Oceanogr. 36, 1763–1785.

Peters, H., Baumert, H.Z., Jacob, J.P., 2005a. Marine turbulence: theories, observations and models. Cambridge University Press (Chapter 39).

Peters, H., Johns, W.E., Bower, A.S., Fratantoni, D.M., 2005b. Mixing and entrainment in the Red Sea outflow plume. part i: Plume structure. J. Phys. Oceanogr. 35, 569–583.

Price, J.F., Baringer, M.O., 1994. Outflows and deep water production by marginal seas. Progress in Oceanography 33, 161–200.

Rodi, W., 1980. Turbulence models and their application in hydraulics. Tech. rep., Institute of the Association for Hydraulic Research, Delft, The Netherlands.

Ruprecht, A., Helmrich, T., Buntić, I., 2003. Conference on modelling fluid flow (cmff03). In: The 12th International Conference on Fluid Flow Technologies. Budapest, Hungary, September.

Sagaut, P., 2005. Large Eddy Simulation for Incompressible Flows, Scientific Computation, An Introduction, third ed. Springer-Verlag, Berlin.

Simpson, J.E., 1987. Gravity Currents in the Environment and the Laboratory. John Wiley and Sons.

Sofianos, S.S., Johns, W.E., 2001. Wind induced sea level variability in the Red Sea. Geophys. Res. Lett. 28 (August), 3175–3178.

Stern, M.E., 1960. The "salt fountain and thermohaline convection. Tellus 12, 172–175.

Umlauf, L., Burchard, H., 2005. Second-order turbulence closure models for geophysical boundary layers. a review of recent work. Cont. Shelf Res. 25, 795–827.

Warner, J.C., Sherwood, C.R., Arango, H.G., Signell, R.P., 2005. Performance of four turbulence closure methods implemented using a generic length scale method. Ocean Modell. 8, 81–113.

Warren, B.A., 1981. Deep circulation of the world ocean. In: Evolution of Physical Oceanography, Scientific Surveys in Honor of Henry Stommel. The MIT Press.

Xu, X., Chang, Y.S., Peters, H., Özgökmen, T.M., Chassignet, E.P., 2006. Parameterization of gravity current entrainment for ocean circulation models using a high-order 3d nonhydrostatic spectral element model. Ocean Modell. 14, 19–44.

Zalesak, S.T., 1978. Fully multidimensional flux-corrected transport algorithms for fluids. J. Comput. Phys. 31, 335–362.